5

Advanced Applications of Numerical Weather Prediction Models – Case Studies

P.W. Chan
Hong Kong Observatory
Hong Kong, China

1. Introduction

Numerical weather prediction (NWP) models are widely used nowadays in weather forecasting services. The models that are commonly considered include the global models and the mesoscale models with horizontal resolutions in the order of several kilometres to a couple of tens of kilometres. Performance of NWP models with even higher spatial resolutions is studied extensively recently with the objective of making location-specific forecasts. This paper describes some attempts of modelling the weather conditions in Hong Kong, a subtropical, coastal city, with a horizontal resolution of a kilometre or less, and presents the applications of the model results in the forecasting of hazardous weather. The following aspects are included:

a. Turbulence forecasts – Turbulence could be hazardous to the aircraft (HKO, IFALPA and GAPAN, 2010). At the Hong Kong International Airport (HKIA), terrain disruption of the prevailing wind is the main case of airflow disturbances experienced by the pilots. Simulations of the wind flow down to a horizontal resolution of 50 m have been tried out to study the possibility of providing an indication of the occurrence of terrain-induced turbulence. Moreover, the simulated turbulence intensity is compared with the measurements by sophisticated remote-sensing meteorological instruments, including minisodar, radar wind profilers and Light Detection And Ranging (LIDAR) systems.
b. Wind gust forecast – Strong gust could occur in association with the passage of subtropical squall lines. Terrain effect may also bring about gustiness of the wind. A physical-based approach has been attempted in simulating the gusts in intense convective weather and terrain-induced airflow disturbances. The simulations are carried out with a horizontal resolution of 0.2 to 1 km. In the selected case studies, the simulated gusts are comparable with the actual observations by the dense network of ground-based anemometers in Hong Kong.
c. Strong wind and heavy rain forecast – High winds associated with tropical cyclones and rainstorms due to summer monsoon are hazardous weather to the general public. This paper also discusses the possibility of improving the forecasting of such weather phenomena by using numerical simulations of high spatial resolutions (1 – 2 km) and sophisticated algorithms of assimilating actual observations into the NWP models. In particular, the inclusion of radar data brings about significant improvement in the forecasting of high winds and heavy rain of tropical cyclones.

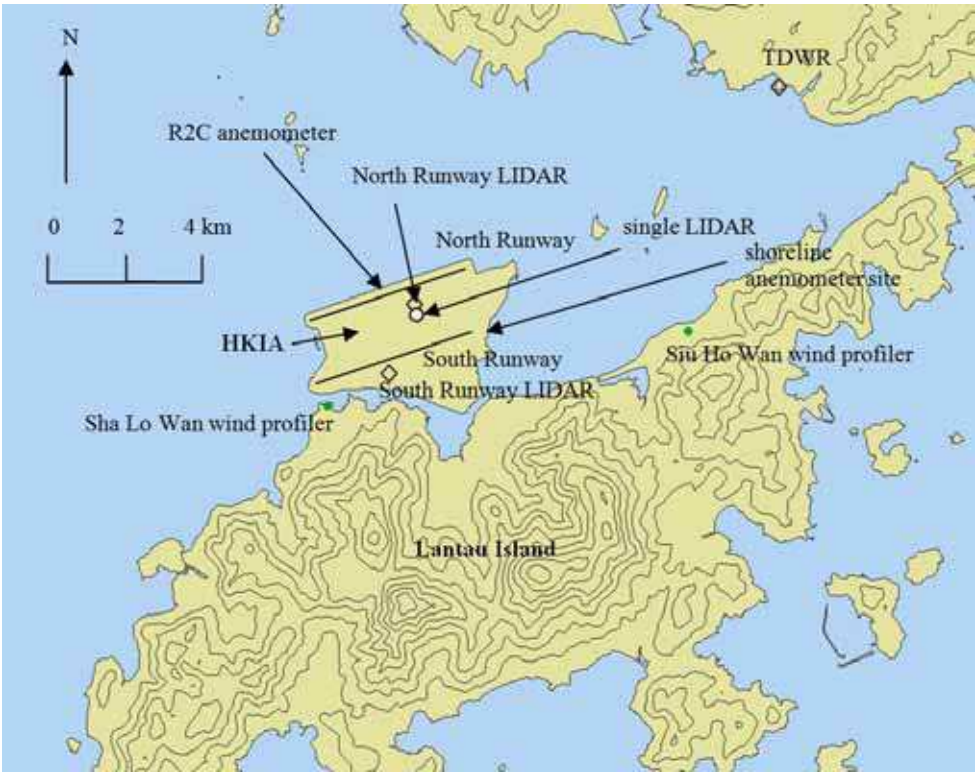

Fig. 1. Locations of the meteorological instruments mentioned in this Chapter. The terrain around HKIA is also shown. Height contours: 100 m. The single LIDAR at the airport (before relocation to become the south runway LIDAR in 2008) is shown as a white dot.

2. Turbulence forecasts

HKIA is situated in an area of complex terrain (Figure 1). To the south of the airport is the mountainous Lantau Island with peaks rising to about 1000 m AMSL and valleys as low as 400 m in between. Turbulent airflow due to terrain disruption could occur in the airport area when the winds from east to southwest climb over Lantau Island. Low-level turbulence (below 1600 feet or 500 m) is an aviation hazard to the aircraft flying into or out of HKIA. It brings about rapid bumps or jolts to the aircraft. In severe turbulence cases, abrupt changes in the altitude and attitude of the aircraft may occur and the pilot may suffer a momentary loss of control.

The Hong Kong Observatory (HKO) provides turbulence alerting services to HKIA. In accordance with the practice of the International Civil Aviation Organization (ICAO), turbulence intensity is expressed in terms of the cube root of the turbulent kinetic energy (TKE) dissipation rate, or eddy dissipation rate (EDR) (ICAO 2007). An $EDR^{1/3}$ between 0.3 and 0.5 $m^{2/3}s^{-1}$ refers to moderate turbulence, and $EDR^{1/3}$ of 0.5 $m^{2/3}s^{-1}$ or above is severe turbulence. Studies have been carried out to measure EDR using remote-sensing instruments such as LIDAR systems (Chan 2006) and radar wind profilers (Chan and Chan

2004) in the airport area for improving the detection of low-level turbulence that may be encountered by the aircraft. The locations of the equipment could be found in Figure 1.

Forecasting of turbulence intensity distribution around HKIA using NWP models would be useful in providing short-term turbulence warnings to the pilots (e.g. in the next several hours). This section examines the feasibility of numerical simulation of the EDR field using the Regional Atmospheric Modelling System (RAMS) (Cotton et al. 2003) in typical cases of turbulent airflow at HKIA by comparison to the EDR measurements from remote-sensing instruments. Numerical simulation of terrain-induced turbulence over Lantau Island has been studied in Clark et al. (1997) with a horizontal resolution of 62 m in a tropical cyclone case. The horizontal resolution of the innermost grid in the present study is of similar magnitude (50 m) and severe turbulence associated with a typhoon is also studied. However, this paper includes the following new features:

a. Instead of initializing the numerical model with a single upper-air ascent and adding excitation artificially into the model, RAMS in this study is nested with the output of an operational mesoscale meteorological model in order to assess the possibility of forecasting the occurrence of severe turbulence over HKIA in an operational model setup;
b. Instead of comparing the model results with the measurements by an aircraft along a flight leg only, more extensive comparison is made in the present study, viz. with the EDR map obtained from a Doppler LIDAR and EDR profile measured by a radar wind profiler; and
c. The impact of different turbulence parameterization schemes on the numerical simulation results is studied.

The latest version of RAMS, viz. version 6, is used in this study. It is nested with the operational Regional Spectral Model (ORSM) of HKO, which has a horizontal resolution of 20 km (Yeung et al. 2005). Four nesting runs are performed with RAMS using the following horizontal resolutions: 4 km, 800 m, 200 m and 50 m (known as grids 1 to 4 respectively). Technical details of the model setup could be found in Chan (2009). The innermost domain (Figure 2(a)) focuses on the area to the west of HKIA, which is downwind of the mountains on Lantau Island in east to southwesterly flow.

In grids 1, 2 and 3, Mellor-Yamada 2.5-level closure scheme (Mellor & Yamada 1982) is used. For grid 4, Deardorff (1980) scheme is employed. It is applied to both vertical and horizontal mixing, so that the turbulence so simulated is isotropic and the diffusion coefficients are the same in all directions. The prognostic TKE equation is solved. The dissipation term in the TKE equation, viz. the EDR (ε), is given by:

$$\varepsilon = \frac{C_D E^{3/2}}{l} \tag{1}$$

where l is a subgrid-scale mixing length which depends on the atmospheric stability (see Deardorff (1980) for details), E the TKE and $C_D = 0.19 + 0.51 l \,/\, (\Delta x\, \Delta y\, \Delta z)^{1/3}$ (Δx is the grid size in the x-direction, etc.).

A case of the passage of Typhoon Imbudo to the southwest of Hong Kong on 24 July 2003 is considered here. This was the day with the largest number of severe turbulence reports from aircraft since the opening of HKIA in 1998 (Chan & Mok 2004). Imbudo brought gale-force southeasterly wind to the airport area. The result of RAMS 3-hour simulation initialized at

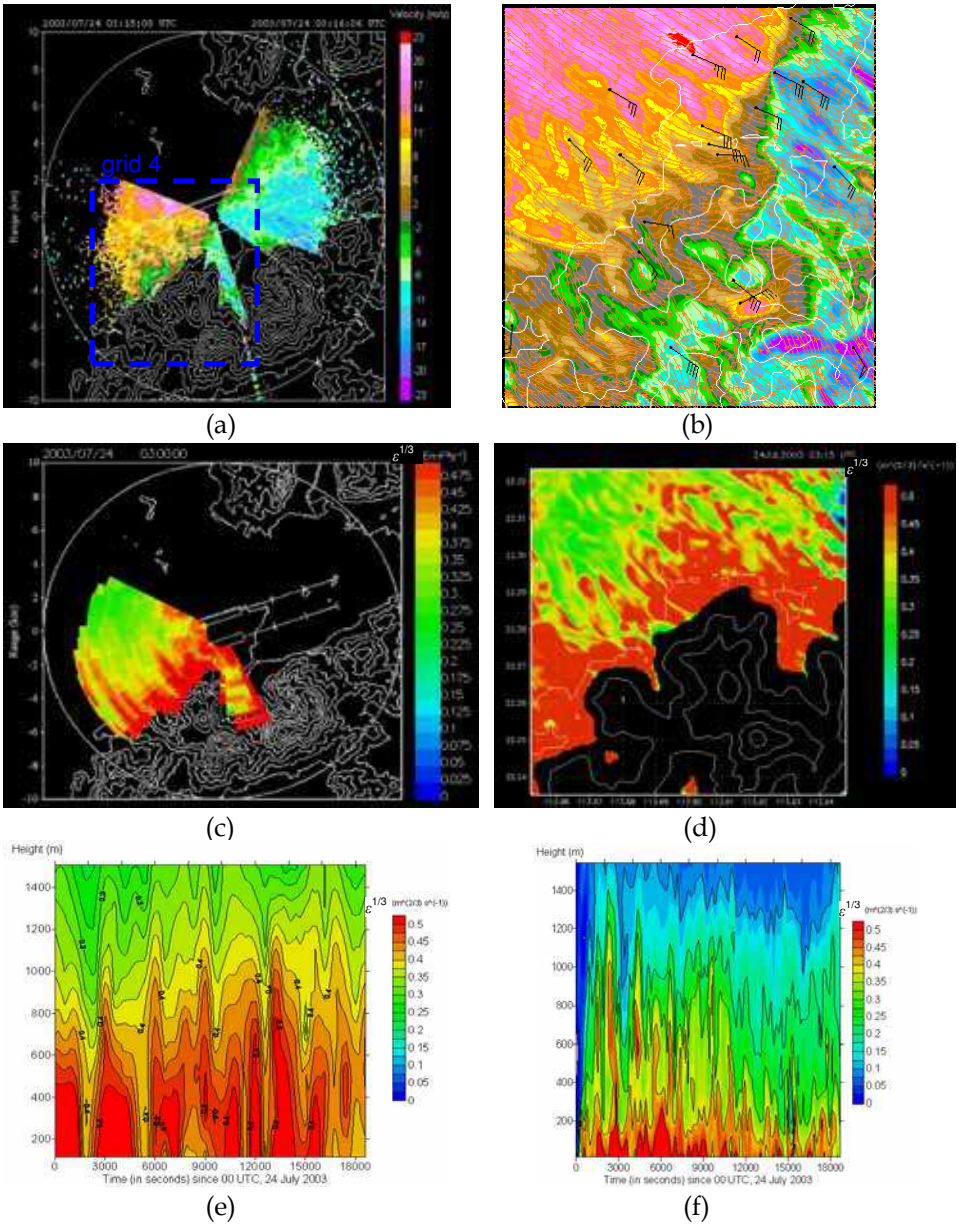

Fig. 2. LIDAR's radial velocity imagery from 1-degree conical scan at 03:15 UTC, 24 July 2003 (a) and the corresponding EDR map based on LIDAR data (c). The RAMS simulation results at the same time of (a) and (c) at 50 m AMSL are given in (b) and (d) respectively. (e) is the observed turbulence intensity from SLW wind profiler, and the simulated results are in (f).

00 UTC of 24 July (Figure 2(b)) is similar to the LIDAR's radial velocity imagery at 03:ISUTC, 24 July, (Figure 2a) except that the blobs of reverse flow (coloured green in Figure 2(a)) to the west of HKIA extended further downstream of Lantau Island in reality. There were streaks of severe turbulence (coloured red in Figure 2(c)) extending for about 4 km from the mountains on Lantau Island. These streaks are well captured in the model prediction (Figure 2(d)).

The model-simulated turbulence intensity has about the same magnitude as the measurement from the wind profiler in the first couple of hundred metres above ground (c.f. Figures 2(e) and 2(f)). Further aloft, it decreases too rapidly with height when compared to actual observations. Fast and Shaw (2002) reported similar discrepancies in the RAMS simulations for the Vertical Transport and Mixing (VTMX) campaign at Salt Lake Valley, U.S.A. using Mellor-Yamada 2.5-level closure scheme. They conjectured that the differences might be due to over-prediction of vertical mixing near the ground and under-prediction of TKE aloft in the model simulations. The latter behaviour was also observed in simulations using the Deardorff scheme (Trini Castelli et al. 2005). Nonetheless, in the present simulations, it is interesting to note that the model simulated results suggest that moderate to severe turbulence can penetrate to a height of about 1000 m at times, similar to the wind profiler observations.

3. The use of other turbulence parameterization schemes

Apart from Deardorff (1980) scheme, other turbulence parameterization schemes that are developed recently are also available RAMS version 6. It would be interesting to study other the model simulation results depend on the selection of the turbulence scheme. One such scheme is the TKE-mixing length (e-l) scheme. In this scheme, the diffusion coefficient of momentum K_m is determined as:

$$K_m = c_\mu E^{1/2} l \tag{2}$$

where c_μ is a closure empirical constant. Following Xu and Taylor (1997), it has a value of 0.41. This constant is in turn related to the corresponding empirical constant of dissipation term of TKE $\varepsilon_\mu = c_\mu^3$. In the present study, c_μ is made variable between 0.1 and 0.7 and the resulting $EDR^{1/3}$ field is compared with the actual measurements (mainly vertical EDR profiles from the two radar wind profilers near HKIA) to find out a suitable value for this empirical constant.

Moderate easterly winds prevailed along the southern coast of China on 3 December 2008. From the radiosonde ascents at 00 and 12 UTC on that day (not shown), temperature inversion (of a few degrees) or an isothermal was depicted between about 600 m and 900 m above ground. From the LIDAR's velocity imagery (Figure 3(a)), easterly flow prevailed in the area of the airport. However, a region of weaker and possibly reverse flow appears to the southwest of HKIA (shown as grey in Figure 3(a)). The occurrence of such a region is possibly related to the airflow disruption by the complex terrain of Lantau Island in a stable boundary layer.

The model simulation starts at 00 UTC, 3 December 2008 and the results at 05:30 UTC on that day are analyzed here. The model-simulated wind field using the e-l scheme with $c_\mu = 0.4$ is shown in Figure 3(b). It could be seen that, apart from the generally easterly flow, there is an area of southerly flow to the west of the HKIA. The occurrence of the latter is generally consistent with the Doppler velocity field measured by the LIDAR (Figure 3(a)), though the spatial extent of the southerly flow (arising from terrain disruption) may be exaggerated.

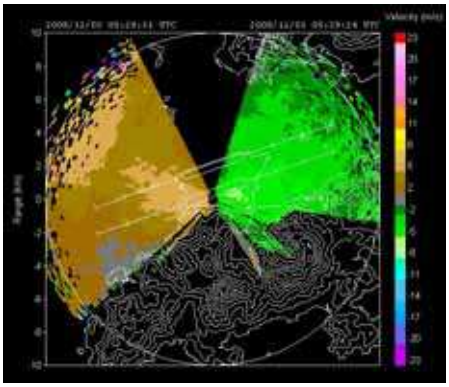

(a)

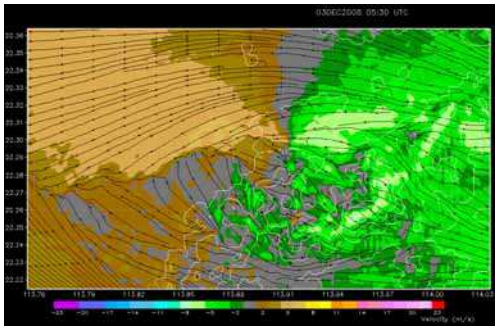

(b)

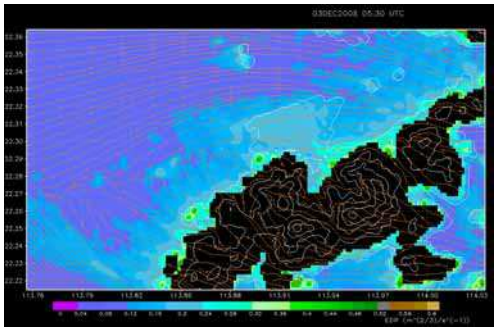

(c)

Fig. 3. The winter monsoon case at 05:30 UTC, 3 December 2008. (a) is the velocity imagery from the south runway LIDAR. The model-simulated winds (resolved along the LIDAR's radials) at a height of 50 m are shown in (b). The $EDR^{1/3}$ field at the same time from model simulation is given in (c).

The model-simulated $EDR^{1/3}$ field at that time is given in Figure 3(c). More turbulent air is forecast downstream of Lantau Island. The result appears to be reasonable considering the mechanical generation of turbulence as the airflow impinges on Lantau terrain.

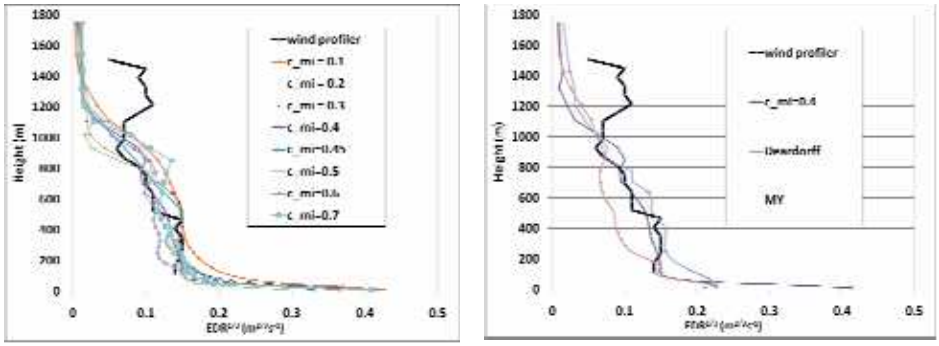

best performing: c_mi = 0.4

(a)

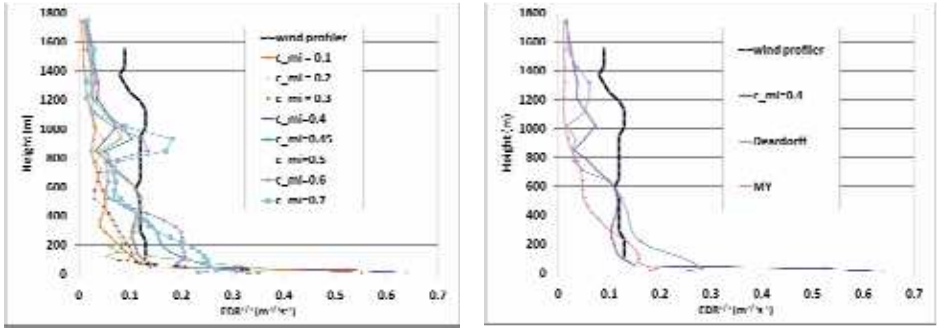

best performing: c_mi = 0.4

(b)

Fig. 4. The $EDR^{1/3}$ profiles from the wind profiler at (a) Sha Lo Wan and (b) Siu Ho Wan in comparison with the model-simulated profiles using the various turbulence parameterization schemes: c_mi is the c_μ value in e-l scheme, Deardorff means Deardorff turbulence scheme, and MY is the Mellor-Yamada 2.5 scheme available in RAMS 6.0.

The $EDR^{1/3}$ profiles at Sha Lo Wan (SLW) and Siu Ho Wan (SHW) are qualitatively compared with model-simulation results in Figures 4(a) and (b) respectively. The locations of these two wind profilers could be found in Figure 1. The e-l scheme and Deardorff scheme give $EDR^{1/3}$ values that are generally consistent with the actual observations up to about 1000 m. At higher altitudes, the forecast $EDR^{1/3}$ values fall with height too rapidly. On the other hand, the Mellor-Yamada scheme in generally gives too small $EDR^{1/3}$ values in various altitudes. It is interesting to note that, for e-l scheme, if c_μ is taken to have a too low value (e.g. 0.1), the resulting $EDR^{1/3}$ curve is quite close to the wind profiler data at SLW, but not at SHW.

The root-mean-square (r.m.s.) differences between the model-simulated results and the actual measurements of $EDR^{1/3}$ between 120 m and 1500 m (the first and the last range gates of the wind profilers in low mode) have been calculated as a function of c_μ. The results for SLW and SHW are given in Figures 5(a) and (b) respectively. It could be seen that:

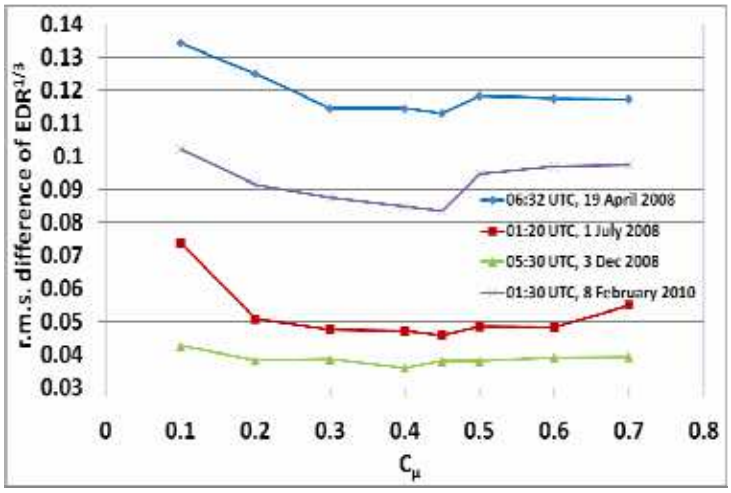

(a)

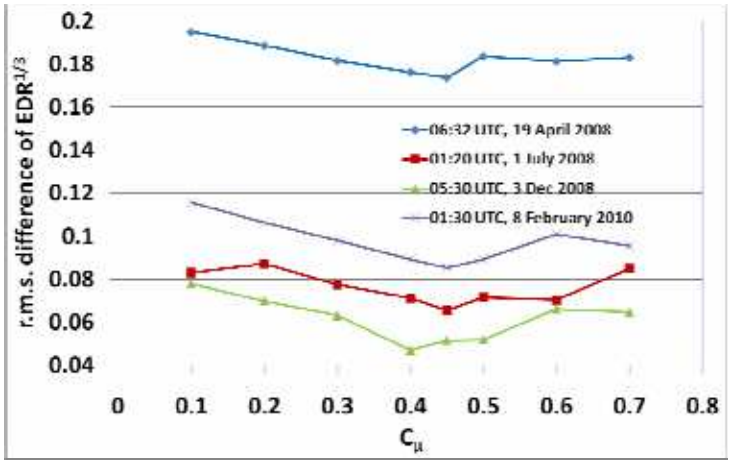

(b)

Fig. 5. The r.m.s. difference between model-simulated and actual measurement of $EDR^{1/3}$ as a function of c_μ value in e-l scheme for the wind profiler at (a) Sha Lo Wan and (b) Siu Ho Wan. Four cases are considered in the figure.

i. The "optimal" c_μ value giving the smallest r.m.s differences is about 0.4 to 0.45. This is consistent with the results in the literature (between 0.40 and 0.55).
ii. The r.m.s. differences are much greater for the tropical cyclone case (19 April 2008) than the other cases, such as the moderate wind case (3 December 2008).

	Mellor-Yamada	Deardorff	e-l scheme (best performing)
19 April 2008	0.172	0.123	0.113
1 July 2008	0.102	0.041	0.046
3 December 2008	0.043	0.034	0.036
8 February 2010	0.154	0.121	0.083

(a) Sha Lo Wan

	Mellor-Yamada	Deardorff	e-l scheme (best performing)
19 April 2008	0.199	0.173	0.174
1 July 2008	0.103	0.073	0.066
3 December 2008	0.071	0.060	0.047
8 February 2010	0.127	0.120	0.085

(b) Siu Ho Wan

Table 1. The r.m.s. differences between the model-simulated $EDR^{1/3}$ profiles and the actual measurements from the wind profiler at (a) Sha Lo Wan and (b) Siu Ho Wan for the various turbulence parameterization schemes.

The r.m.s. differences for e-l scheme are compared quantitatively with those for Deardorff scheme and Mellor-Yamada scheme, as shown in Table 1. It could be seen that, using an optimal value of c_μ, the use of e-l scheme with a variable asymptotic mixing length gives results that are comparable with the best turbulence parameterization scheme, namely, Deardorff scheme, as found out in the previous study of Chan (2009). The major challenge for e-l scheme would then be the instability in strong wind situation (e.g. tropical cyclone case). On the other hand, Mellor-Yamada scheme generally gives too small $EDR^{1/3}$ values and thus the r.m.s. differences are the largest among the three schemes.

For e-l scheme and Deardorff scheme, the r.m.s differences with actual observations are generally in the order of 0.03 – 0.07 $m^{2/3}s^{-1}$ in moderate wind situation. This is still less than 0.1 $m^{2/3}s^{-1}$. As such, the forecast $EDR^{1/3}$ fields by these turbulence parameterization schemes could be useful in the monitoring of low-level turbulence in an area of complex terrain, which is a safety hazard to the aircraft. On the other hand, the performance in tropical cyclone cases is more questionable. The simulation results for Deardorff scheme could still be useful for the monitoring of low-level turbulence in the first few hundred metres or so, as discussed in Section 2 and Chan (2009).

In Chan (2009), a fixed vertical gridding is used for all model simulations, namely, with a stretching ratio of 1.15 according to the vertical gridding method of RAMS. As an illustration of the potential effect of vertical gridding on the simulation results of turbulence intensity profile, a case study is considered in this paper, namely, moderate southerly winds in the morning of 1 July 2008 under the summer monsoon. Moreover, for simplicity, only the Deardorff scheme is used in this case study. Three vertical griddings have been used, namely, with a stretching ratio of 1.15, 1.35 and 1.55.

The $EDR^{1/3}$ distribution obtained from LIDAR data at 01:18 UTC, 1 July 2008 is shown in Figure 6(a). Due to the mountains on Lantau Island, the area of moderate turbulence extends up to about 6 km downstream of this island. However, at the same time there are some "narrow streaks" of lower turbulence, reaching the level of light turbulence only (coloured

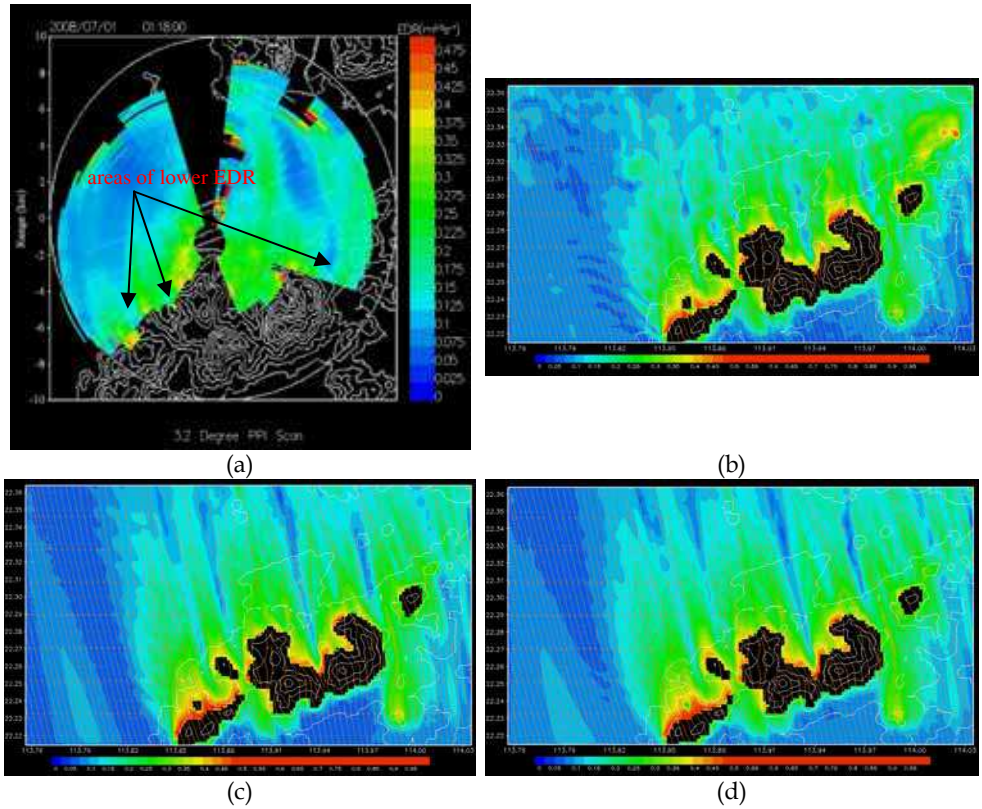

Fig. 6. (a) is the LIDAR-estimated $EDR^{1/3}$ distribution in the vicinity of the airport at 01:18 UTC, 1 July 2008. The model-simulated results are given in (b), (c) and (d), corresponding to the use of vertical grids with the stretching ratio 1.15, 1.35 and 1.55 respectively.

blue in Figure 6(a)). They appear to originate from the gaps of Lantau Island. As such, the mechanical turbulence associated with the cross-mountain flow brings about moderate turbulence to the areas in the vicinity of the airport, but at the same time the airflow through the gaps has light turbulence only.

The above features of turbulence distribution could largely be reproduced from RAMS simulations. The simulated $EDR^{1/3}$ patterns with different vertical griddings are very similar, as shown in Figures 6(b) to (d). The height of about 300 m is considered in the model simulations, which is about the height of the location of light turbulence gap flow to the east of the airport.

Though the general turbulence patterns are largely the same, the magnitudes of the simulated $EDR^{1/3}$ values could be quite different with the use of the different vertical griddings. The forecast $EDR^{1/3}$ profiles from the three grids are compared with the actual measurements from SLW and SHW wind profilers in Figure 7. It could be seen that the vertical gridding used in the study so far and in Chan (2009), namely, a stretching ratio of 1.15, gives the best comparison results with the actual data. With coarser vertical grids, the $EDR^{1/3}$ values tend to be over-forecast.

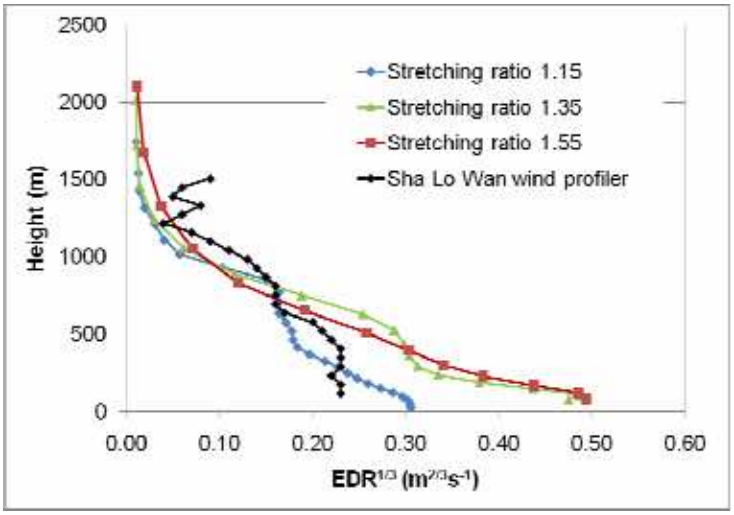

(a)

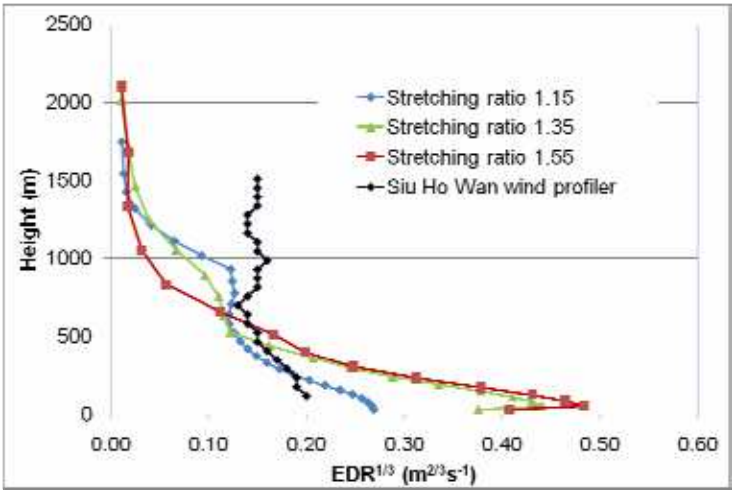

(b)

Fig. 7. Comparison between $EDR^{1/3}$ obtained from the wind profiler and the simulation results for (a) Sha Lo Wan, and (b) Siu Ho Wan. The model simulations include the use of vertical co-ordinates with stretching ratios 1.15, 1.35 and 1.55.

The studies so far concentrate on $EDR^{1/3}$, which is the intentionally adopted metric for turbulence intensity in aviation application. Other metrics have been considered for aviation purpose, such as TKE. The performance of RAMS in the simulation of TKE has also been examined in a couple of examples. Deardorff scheme is employed in all the simulations.

The first example is the spring-time easterly wind case on 8 February 2010. The model-simulated TKE profiles at shoreline anemometer site (location in Figure 1) with different vertical griddings (namely, stretching ratios of 1.15, 1.35 and 1.55) are shown in Figure 8(a).

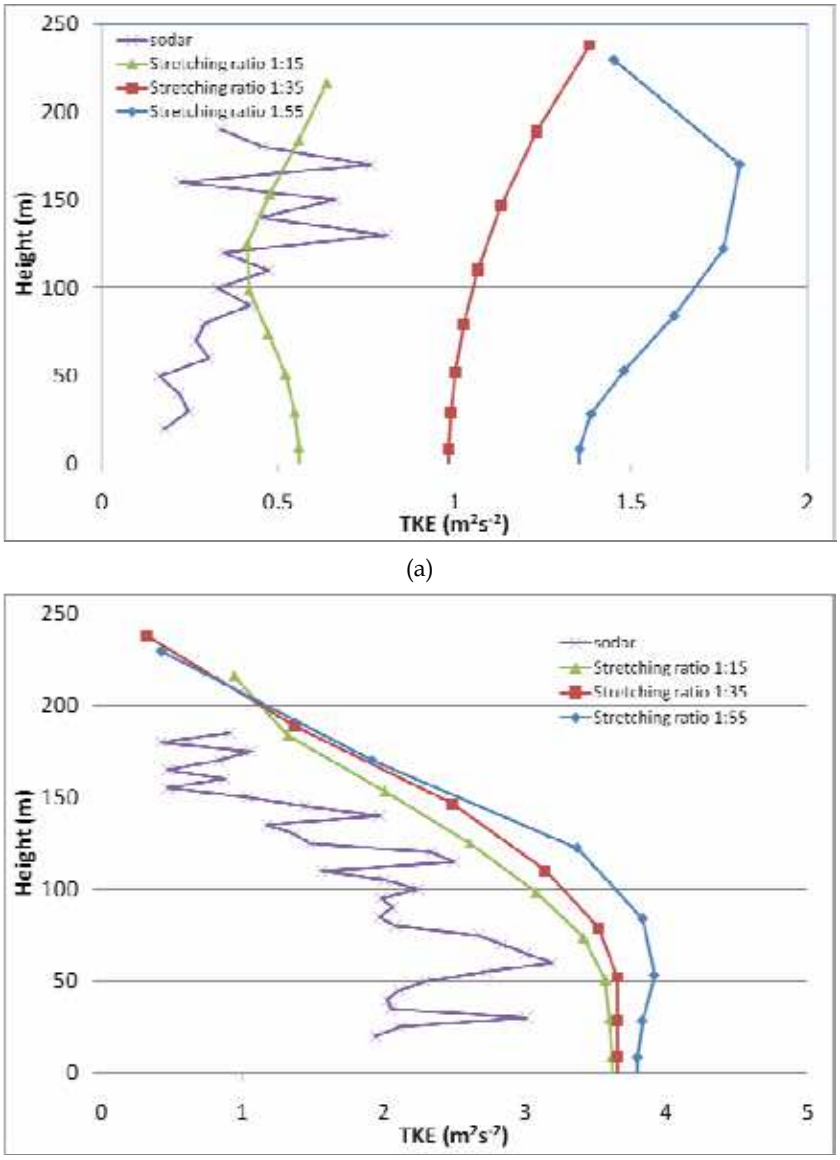

(a)

(b)

Fig. 8. TKE profile measured by the sodar at shoreline anemometer site and compared with the model simulated results: (a) 03 UTC, 8 February 2010, and (b) 07 UTC, 5 March 2010.

It appears that, with the use of a coarser grid, the TKE tends to be higher within the first couple of hundred metres or so above ground.

In order to assess the quality of the model-simulated TKE, the actual measurements by the minisodar at shoreline anemometer site has been considered. Data are available up to about

200 m above sea level, and they are plotted in Figure 8(a). Simulation is carried out starting from 00 UTC, 8 February 2010 and the simulation results after three hours are used. The simulated TKE profile with a vertical gridding of the stretching ratio of 1.15 seems to be generally consistent with the actual measurements. This comparison result supports the use of the stretching ratio of 1.15 for the vertical gridding in the simulation study for easterly flow.

Another case is considered here, namely, stronger turbulence in the southerly wind case of 5 March 2010. Simulation is carried out starting from 00 UTC, 5 March 2010 and the simulation results after 7 hours are considered. The sodar-measured profile and the model-simulated profile of TKE are compared in Figure 8(b). Again, the actual profile appears to be captured well by the model simulation (Deardorff scheme, stretching ratio of 1.15 for the vertical gridding), though the simulated results have higher values of TKE. The simulation results based on the stretching ratio of 1.15 for vertical gridding have the best comparison with the actual observations, which supports the selection of this stretching ratio value.

The minisodar with a measurement range of 200 m has been working at the airport since January 2010. More data would be collected for assessing the performance of RAMS simulations of TKE, e.g. in summer monsoon and tropical cyclone situations.

4. Wind gust forecast

Wind gust is an important element in the forecasting of local weather. It could have significant impact on the safety of the public and the operation of certain business such as container port and construction work. The destruction associated with the gusts may be much larger than the mean wind itself, particularly in conditions when the mean wind is light. People working in the exposed area may need to take prompt action within a short period of time in order to protect themselves against the impact of gusty winds. For instance, on 9 May 2005, a squall line along coastal area of southern China brought strong gusts to Hong Kong. At the container port of the territory, some empty containers were blown to collapse under the gust, causing one death and two injuries. In aviation meteorology, gust could have great impact on the operation of the airport, particularly in strong crosswind situation when the pilots may need to make difficult decisions in attempting to land on a runway. Accurate forecast of the gust, such as in tropical cyclone situation, would facilitate the smooth operation of the airport in strong crosswind and minimize air traffic disruption.

Traditionally, wind gust estimate is mainly based on climatological information of the wind excess due to gust on top of the mean wind in different weather conditions. In a subtropical coastal area like Hong Kong, gust climatology may be formulated in synoptic patterns like northeast monsoon in the winter, strong easterly winds under stable boundary layer in the spring, southwest monsoon in the summer, intense convectice weather like squall lines, and tropical cyclone situations. Wind gust forecasting is more challenging at HKIA due to the complex terrain in the vicinity. Winds from east to southwest may be disrupted by the terrain and give rise to strong gusts in favourable weather condition. As a result, gust forecasting not only needs to consider the synoptic weather pattern, but also takes into account the mesoscale and even microscale features as well such as convective rain cells and terrain-induced airflow disturbances.

This section aims to study the possibility of using a more objective estimation method of wind gust given the complicated condition at HKIA. The basis is a NWP model with high

spatial resolution, and a physical approach to wind gust estimate. The RAMS version 4.4 is employed. It has been found to give satisfactory results in the simulation of microscale airflow disturbances and turbulent winds arising from the complex terrain of Lantau Island. In the simulation of a squall line case, the horizontal resolution down to 1.33 km is employed in the present study in order to resolve the convection explicitly. For terrain-disrupted airflow, the resolution is increased further to 200 m so that the complex terrain of Lantau Island could have a reasonable representation in the numerical model. The wind gust estimate is based on turbulent kinetic energy and vertical air motion from the RAMS simulation results (Brasseur 2001).

A trough of low pressure affected the inland area of southern China in the morning of 9 May 2005. A squall line developed in the strong southwesterly flow ahead of the trough and moved southeastward to Hong Kong. It swept across the territory between noon and 1 p.m. (Hong Kong time, which is 8 hours ahead of UTC), bringing gusts of about 20 m/s to HKIA and more than 30 m/s to some other places in Hong Kong (Figure 9(a)). The largest gust was recorded at the container terminal at Kwai Chung (location in Figure 9(a)), reaching 37.6 m/s. A more detailed account of the event could be found in Lam and Lam (2006).

On the radar display, a bow-shaped echo was observed when the squall line moved across Hong Kong (Figure 9(b)). Strong southwesterly wind prevailed at the surface ahead of this intense radar echo with northwesterly flow at its rear (not shown). The passage of the squall line at a location showed up as a rapid change of the wind direction (from southwesterly to northwesterly) and a sharp peak in the wind speed (associated with the squall) in a matter of several minutes. In a typical wind trace of an anemometer (not shown), the southwesterly flow ahead of the squall line was rather gusty, with a mean wind of about 10 m/s and the gust reaching 16 m/s or so. The squall line moved past that anemometer at about 12:18 p.m. and the gust reached a maximum of 21 m/s in the northwesterly flow. The wind remained northerly for about half an hour afterwards, and became significantly weaker and less gusty. The temperature also dropped from a high of 27°C to about 21°C. This was the period when the cold pool behind the squall line affected the territory. Starting from around 1:20 p.m., winds turned to southeasterly and the temperature rose again after the passage of the cold pool.

The RAMS simulation reproduces reasonably well the southeastward movement of the squall line. In the "radar" plot of the simulated surface rainfall (Figure 10(a)), an intense, bow-shaped "echo" is forecast to sweep across Hong Kong between noon and 1 p.m. of 9 May 2005, consistent with the actual observations. The updraft in this "echo" reaches a maximum of about 16 m/s (Figure 10(b)), which is the magnitude to be expected in such a severe squall event.

At the surface, the model successfully simulates the strong southwesterly flow ahead of the squall line and the northwesterly flow at the rear of it. For instance, northwesterly wind of 15 m/s (29 knots) is predicted over HKIA after the passage of the squall line (Figure 11(a)), consistent with the actual measurements. At the location of the R2C anemometer at HKIA (location in Figure 1), the wind direction change and the peak in wind speed associated with the squall line are reasonably well forecast (Figure 11(b)). However, some discrepancies are observed between the actual and the forecast wind fields: (a) the arrival time of the squall line is later by about half a hour in the simulation, and (b) the cold pool behind the squall line is more widespread (not shown) and affects Hong Kong for much longer time in the model, e.g. the wind at HKIA (Figure 11(b)) remains to be southwesterly to northwesterly for a couple of hours after the passage of the squall line.

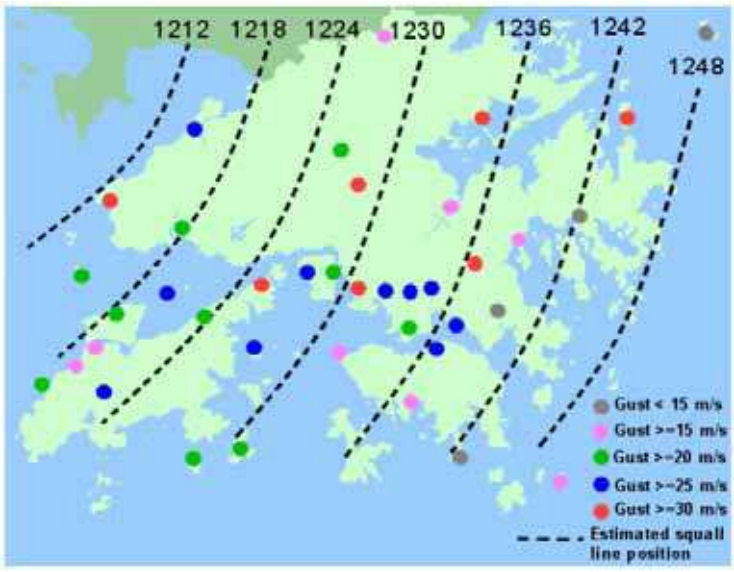

(a)

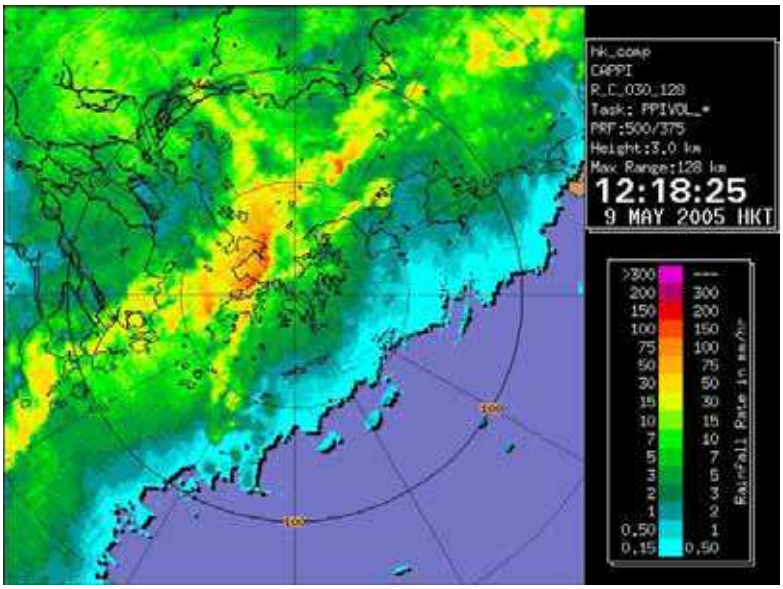

(b)

Fig. 9. (a) shows the location of the squall line in the 9 May 2005 event and the gust measured at various places in Hong Kong due to the squall line. The numbers at the broken curves are in Hong Kong time. (b) is the 128-km range radar picture of Hong Kong at 12:18 p.m., 9 May 2005, showing the passage of the squall line across the territory.

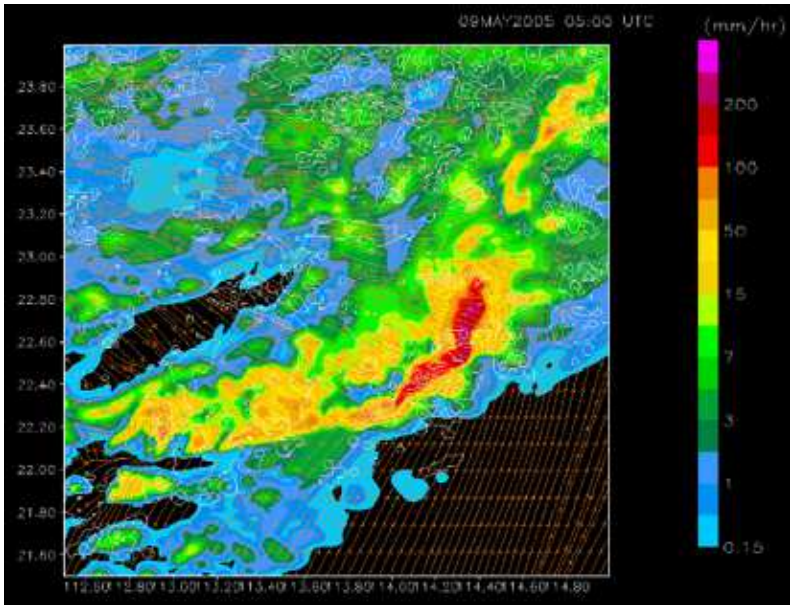

(a)

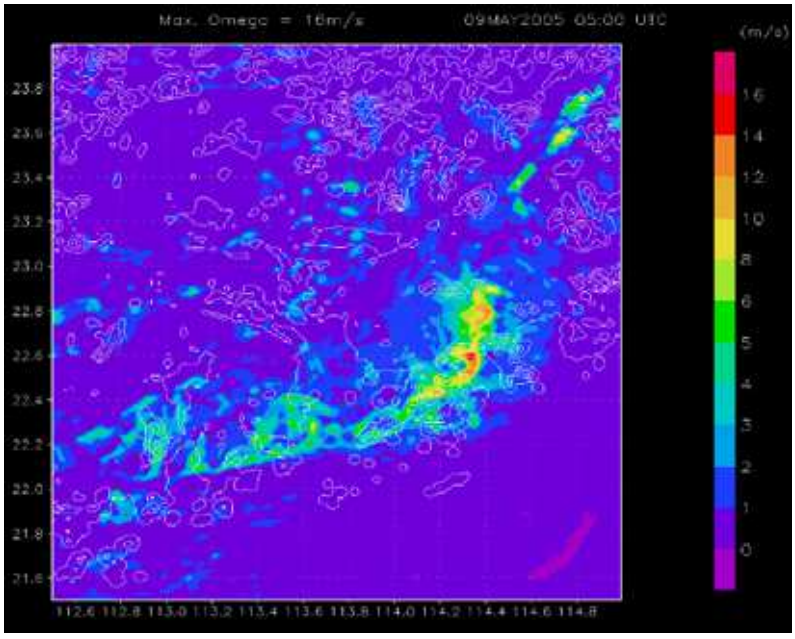

(b)

Fig. 10. (a) is the "radar" plot of the simulated surface rainfall in Grid 2 of RAMS simulation at 1 p.m., 9 May 2005. (b) is the maximum updraft strength simulated using RAMS

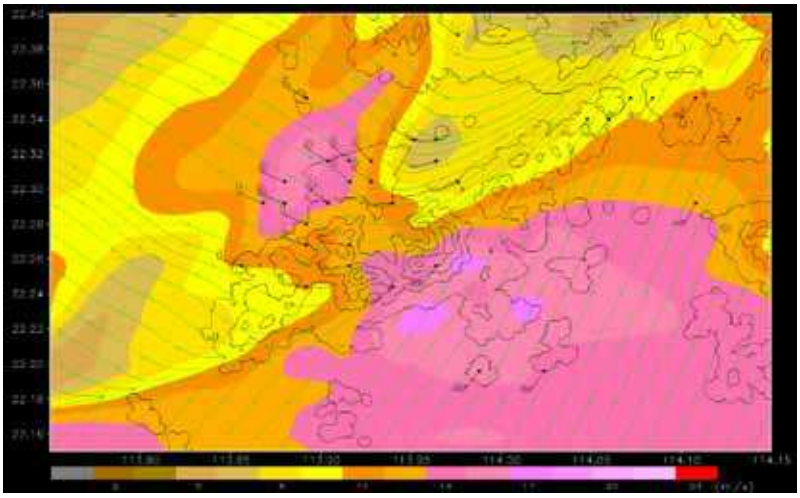

(a)

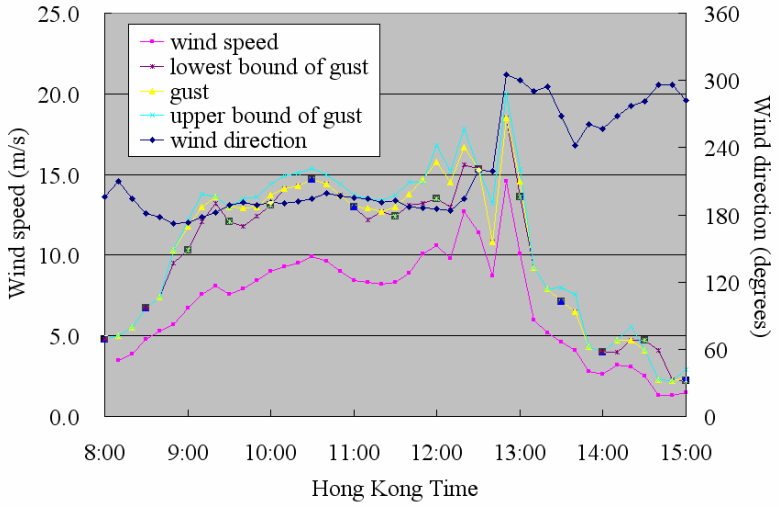

(b)

Fig. 11. (a) is the simulated surface wind magnitude (colour shaded), streamlines (green lines) and winds at the anemometer locations (wind barbs) at 12:50 p.m., 9 May 2005. (b) is the simulated surface wind speed and direction from RAMS and the wind gust estimate from the Brasseur (2001) method at the location of R2C anemometer at HKIA.

Within the Hong Kong territory, the upper bound of the wind gust has a maximum value of 30 m/s based on the simulation results. Though it is smaller than the actual maximum gust observed (37.6 m/s), the gust estimate nonetheless provides a useful indication about the gust that could be attained in the present severe squall event (see the magnitude of gust in various places in Hong Kong in Figure 9(a)). Lam and Lam (2006) found that GUSTEX of

Geerts (2001) gave a wind gust estimate of 25.2 m/s for the present event, which is even smaller than the gust estimated from the Brasseur (2001) method based on RAMS simulation. They proposed a modified GUSTEX using the wind at 700 hPa and the estimated gust value is closer to reality.

An experiment has also been carried out by retaining the default setting of cloud-top turbulent mixing in the simulation. The convective development turns out to be weaker. The maximum updraft is 12 m/s only, which is smaller than that in the model run without the cloud-top mixing. The arrival time of the squall line at Hong Kong is also later by an hour, with weaker northwesterly wind behind the squall line (14 m/s). The cloud-top turbulent mixing appears to have significant effect on the development of convection, the speed of propagation as well as the strength of rear inflow of the squall line in the simulation.

We then turn to the forecasting of gusts in terrain-disrupted airflow. A typical example is studied here. A ridge of high pressure developed over southeastern China later on 10 April 2008 and extended southwards on the following day. Surface easterlies strengthened at HKIA at about 6 a.m. on 11 April. Low level winds veered to the south at around 600 m as depicted by wind profiler data. The cool easterlies were shallow and a low level inversion developed between 400 and 800 m after the onset of easterlies (not shown). From the vertical profile of low level winds in the upstream and downstream of the Lantau Island (not shown), strengthening of low level southeasterly winds from around 10 m/s to 15 m/s was found between 200 m and 800 m when they passed over the hills over Lantau Island with height close to that of the inversion. The timing and strength of the strong low level southeasterlies matched with those of the observed maximum gusts at HKIA during 9 a.m. to 1 p.m. on 11 April.

The strong southeasterlies on the hill tops were rather localised over the Lantau Island (Figure 12(a)). The Froude number in this case was found to be 0.7 - 1 (taking the mean wind speed of 10 m/s, the Brunt-Väisälä frequency of 0.02 /s, and the height of hills on the Lantau Island ranging from about 500 m to 900 m). The flow on the upwind side was subcritical. Thinning and acceleration of airflow occurred on the upslope side and attained maximum at the crest when the Froude number was close to 1. In case the Froude number equals to 1 at the crest, the flow will become supercritical and continue to accelerate as it descends the lee side until it adjusts back to the ambient subcritical conditions. The effect of topography apparently plays a significant role to the gusty condition in this type of east to southeasterly flow in the presence of a low level inversion close to the hill top.

The model forecast increasing mean wind and gust about four hours earlier than observed at HKIA in the morning of 11 April (Figure 12(b)). However, the model forecast maximum gust attained at around noon on that day is consistent with the observed data, though the strength is over-estimated by about 2 m/s.

The sensitivity of gust forecasts to the choice of turbulence parameterization scheme has also been studied. In the simulation of strong east to southeasterly flow on 10 - 11 April 2008, gust forecasts from the model run utilizing Deardorff (1980) as the turbulence parameterization scheme are different from those obtained using Mellor-Yamada Level 2.5 turbulence closure scheme. In particular, the peak of maximum gust occurred at around midnight of 10 April could be depicted by the upper bound forecast from the model run using Deardorff scheme, but not the one using Mellor-Yamada Level 2.5 turbulence closure scheme.

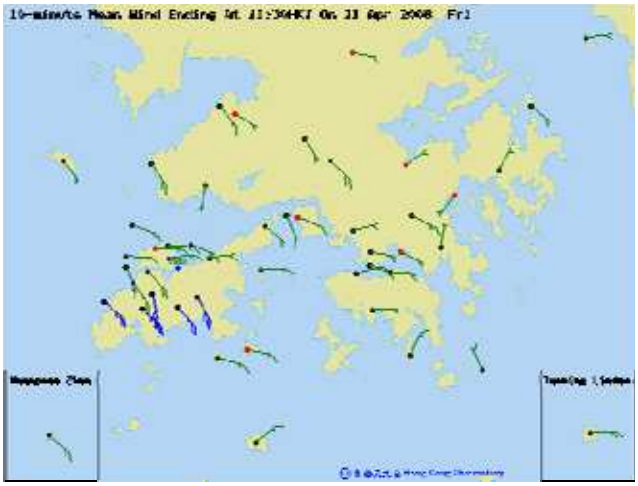

(a)

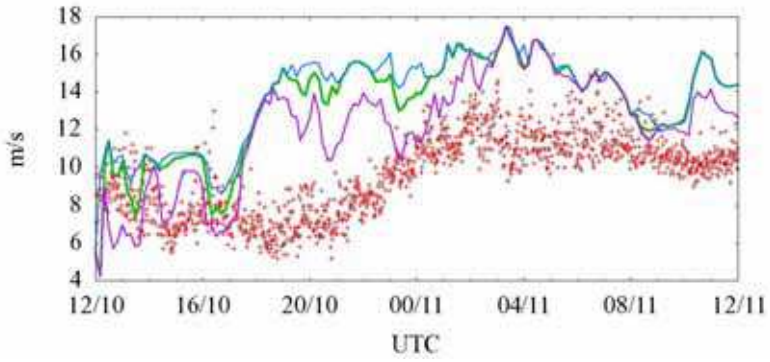

(b)

Fig. 12. (a) is the wind distribution at the surface in Hong Kong at 11:30 a.m., 11 April 2008. (b) is the time series of 24-hour maximum gust forecast by 200-m RAMS with model initial time at 8 p.m. on 10 April 2008: model forecast in green curve, upper bound in blue curve and lower bound in pink curve. This is compared with the maximum value of 1-minute gust (red crosses) among the six anemometers inside HKIA. Local time = UTC + 8 hours.

In the present formulation of the wind gust estimate (see Cheung et al., 2008, for details), the upper bound of gust forecast is given by the maximum wind speed in the boundary layer whose depth is taken as the height where TKE is 0.01 of the surface value. The discrepancy mentioned above for the two turbulence parameterization schemes suggests that they may produce rather different vertical profiles of TKE. The vertical profiles of TKE and wind speed at HKIA extracted from model forecasts at midnight of 10 April 2008 is shown in Figure 13(a). The Mellor-Yamada scheme forecasts the boundary layer top at around 500 m, while that of the Deardorff scheme is around 1400 m. Consequentially, winds of larger speed at higher levels have been taken as the gust upper bound based on the Deardorff scheme (see Figure 13(b)).

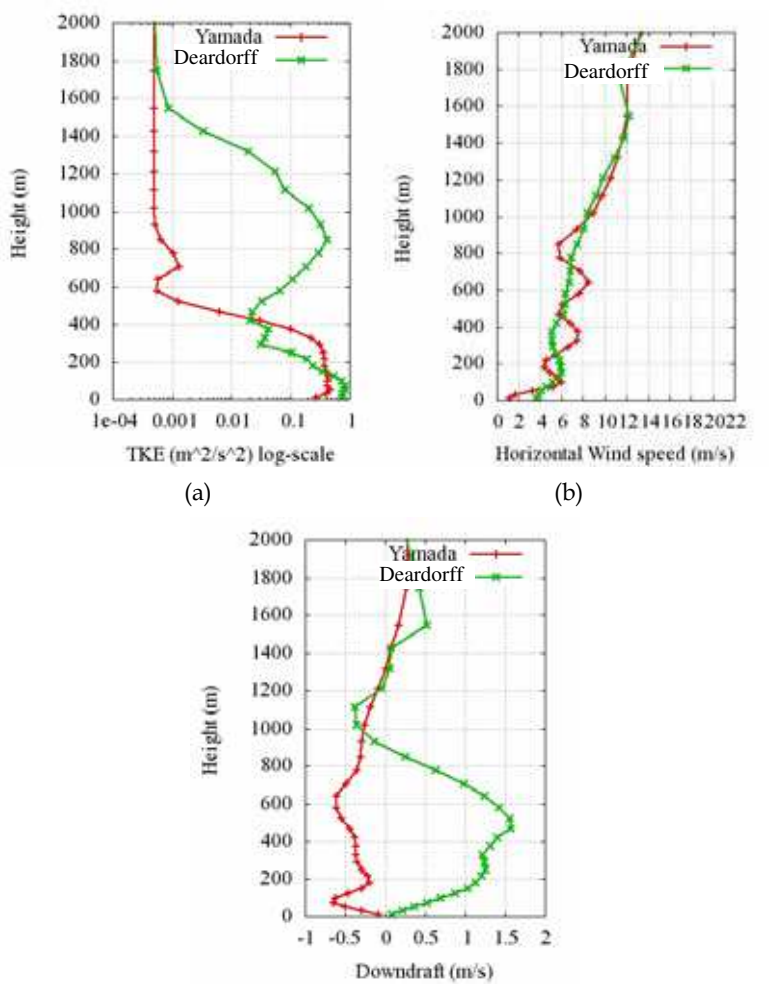

Fig. 13. Vertical profiles of (a) TKE, (b) horizontal wind speed, and (c) downdraft at HKIA at the midnight of 10 April 2008. The TKE plot is in log-scale, red for Deardorff scheme and green for Mellow-Yamada scheme

The vertical profiles of downdraft for the two schemes are also shown in Figure 13(c). The Deardorff scheme successfully depicts the downdraft associated with the accelerated descent of the supercritical air flow from around 500 m while the Mellow-Yamada scheme has no such indication. It should be noted that the downdraft is also considered in the gust estimation as described in Cheung et al. (2008). Further tests would be necessary to obtain more conclusive results for the performance of two turbulence schemes in different types of weather conditions and their impact on the model gust forecasts.

5. High winds and heavy rain associated with tropical cyclones – impact of assimilation of radar data

In every summer, tropical cyclones bring about hazardous weather to south China coastal areas, including strong winds and heavy rain associated with the outer rain bands. Accurate forecasting of the winds and rain caused by tropical cyclones would be very useful for the provision of timely warnings for the general public. Nowadays, NWP models, from synoptic scale to mesoscale scale, are widely used in the weather services in forecasting the heavy rain and strong wind areas brought by tropical cyclones. The performance of NWP models is gradually improved with the physical parameterizations becoming more and more sophisticated. At the same time, the assimilation of remote-sensing data covering the tropical cyclones, such as radar and satellite observations, could also help initializing the NWP models.

In this section, the impact of radar data on the model forecasting of strong wind and heavy rain areas of tropical cyclones is studied. One tropical cyclone event over the northern part of the South China Sea and south China coastal areas in 2008 is considered, namely, Severe Tropical Storm Kammuri in August. At the first step, only the data from a single radar in Hong Kong are used in the analysis. Such data, including the Doppler velocity and reflectivity measurements, are used in a variety of ways, namely, by assimilation using a 3D variational scheme (3DVAR) of the NWP model at the initial time only, by 3DVAR assimilation in a cycling run at two separate times (with 3 hours apart), and in a cycling run but with 3DVAR assimilation of the radar-retrieved 2D wind field. The study aims at finding out which assimilation method has the strongest positive impact on the simulation results, in terms of the forecasting of strong winds and heavy rain areas of the cyclones. The model under consideration is Weather Research and Forecasting (WRF) model version 2.2.

The radar considered in this study is the one located at Tate's Cairn in Hong Kong (22°21′36″N 114°12′54″E). It is an S-band radar at around 585 m AMSL on top of a hill with a Nyquist velocity of 35.8 m/s. It scans at 12 different elevation angles from 0.5° to 34.7°. The volume scan takes about 6 minutes to complete. Before the variational analysis, the radar data are interpolated into a Cartesian grid. The grid has 640 x 640 points with a size of 800 m. In the vertical, the radar data extend from the ground up to 5000 m with a resolution of 500 m.

The Doppler velocity and reflectivity data of Tate's Cairn radar are assimilated into WRF using WRF VAR version 2.1 (Barker et al., 2004). The conventional weather observations, such as surface SYNOP and upper air TEMP/PILOT data, are also included in the analysis. WRF VAR is a variational data assimilation scheme to ingest both conventional and non-conventional data through the iterative minimization of a prescribed cost (or penalty) function. Differences between the analysis and the observations are penalized (damped) according to their perceived error. For simplicity, the errors of radial velocity and reflectivity are taken to be 1 m/s and 1 dBZ respectively. Details of the model setup could be found in Cheung and Chan (2010).

As an experiment, apart from the direct ingestion of Doppler velocity and reflectivity data from the radar, the 2D wind field under the coverage of the radar is retrieved from the Doppler velocity data of the radar and ingested into WRF through WRF VAR. For this purpose, the two-step variational method as described in Yang and Qiu (2006) is employed. In the assimilation into WRF, the 2D wind profile at a grid point is taken to be an "upper-air ascent", similar to the radiosonde measurement.

In the morning of 6 August 2008, Kammuri was located at about 130 km south of Hong Kong and moved to the northwest steadily across the south China coastal waters. It brought about gale-force east to southeasterly winds to Hong Kong. Moreover, the outer rain bands associated with Kammuri affected the coast of Guangdong.

Model simulations start at 00 UTC, 6 August 2008. For cycling run, the first simulation is made at 21 UTC, 5 August 2008 and run for three hours before data assimilation and another model run at 00 UTC, 6 August. The WRF-simulated surface wind magnitude and the streamlines for the various data assimilation runs after 6 hours are shown in Figures 14(a) to (d). The cold-start runs (a) and (b) forecast very strong winds over the territory and seas to the south, reaching 23 m/s or more. On the other hand, the cycling runs (c) and (d) give generally lower wind speeds. In particular, there is just a small area of 23 m/s wind speed (coloured red) in the cycling simulation with the direct assimilation of radar velocity and reflectivity data (Figure 14(c)). Unfortunately there were no surface observations over the seas for direct comparison with the model simulation results. However, if we consider the wind observations over Hong Kong only (Figure 14(e)), the strongest winds seem to be in the order of 17 – 20 m/s (35 – 40 knots) only, and there is no extensive area of surface wind magnitude reaching 23 m/s. Winds of the strength similar with that over Hong Kong were also recorded at Huang Mao Zhou, an island over the northern part of the South China Sea to the south of Hong Kong (not shown).

The rain forecasts of the various model runs are given in Figures 15(a) to (d). Among these runs, the cycling simulation Figure 15(c) gives the stronger rain bands (simulated radar reflectivity of about 40 dBZ) located just to the north of Hong Kong, so that the territory is just clear of the influence of heavier rain. This is the most consistent with the actual radar observation (Figure 15(e)). However, in all simulations, the radar-echo-free area associated with the eye of the tropical cyclone appears to be too large.

It could be seen from the present case that the assimilation of radar data through an advanced data assimilation scheme helps improve the forecasting of high winds and heavy rain of a tropical cyclone. More tropical cyclone cases are under study to see the impact of radar data more systematically.

6. Conclusion

This paper discusses some advanced applications and setup of NWP model in the forecasting of hazardous weather. It is first shown that the use of sub-kilometre simulation and the development of sophisticated turbulence parameterization schemes help the forecasting of turbulence for aviation application, as well as the provision of wind gust estimate in intense severe weather as well as terrain-disrupted airflow. The sub-kilometre simulation is crucial in explicitly forecasting the convection and resolving the complex terrain near the Hong Kong International Airport in fine details in order to capture the terrain-induced airflow disturbances. The forecast results are also shown to be rather sensitive to the choice of turbulence parameterization scheme. In particular, the inclusion of a TKE equation appears to be important in giving a reasonable simulation of the TKE and its dissipation rate.

The assimilation of non-conventional meteorological data, namely, radar data, is shown to improve the forecasting of high winds and heavy rain in a tropical cyclone case. This may be achieved through the use of sophisticated data assimilation scheme, such as 3DVAR of radar reflectivity and radial velocity, or simply direct assimilation of the radar-based 2D wind field retrieved separately.

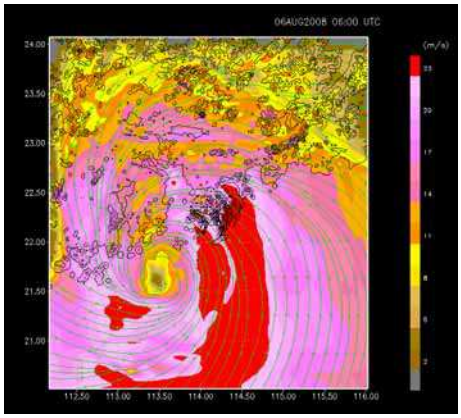

(a) cold start, no radar data

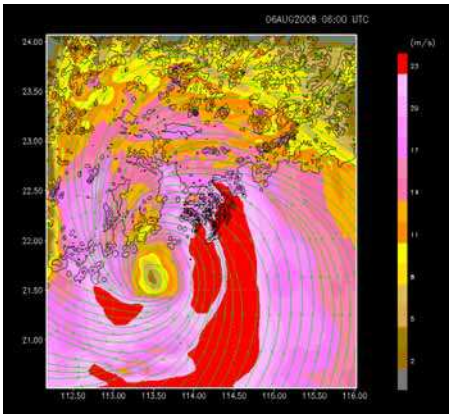

(b) cold start, with the assimilation of radar data

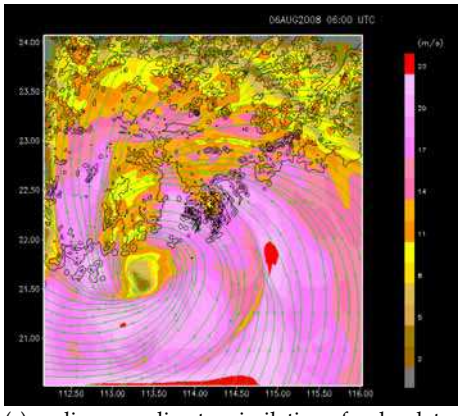

(c) cycling run, direct assimilation of radar data

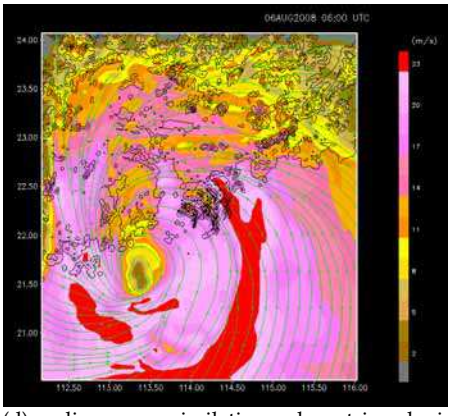

(d) cycling run, assimilating radar retrieved winds

(e) actual surface wind observations in Hong Kong

Fig. 14. The simulated surface wind magnitude (coloured contours) and streamlines for the four different model runs (a) to (d) at 06 UTC, 6 August 2008. (e) shows the actual surface wind data in Hong Kong at the same time.

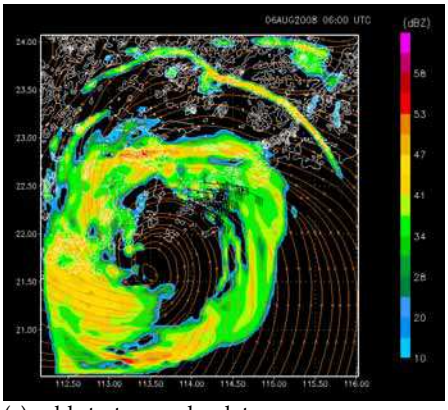

(a) cold start, no radar data

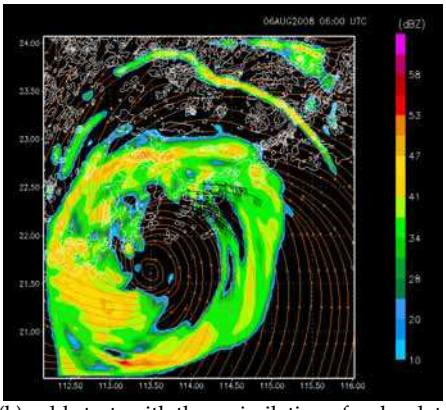

(b) cold start, with the assimilation of radar data

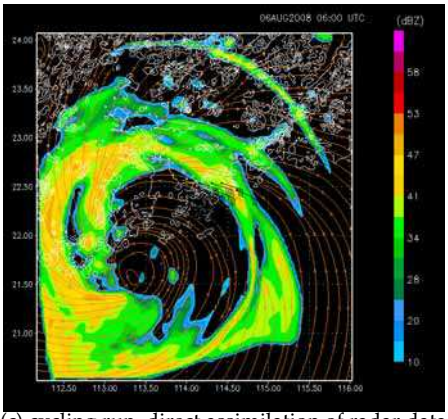

(c) cycling run, direct assimilation of radar data

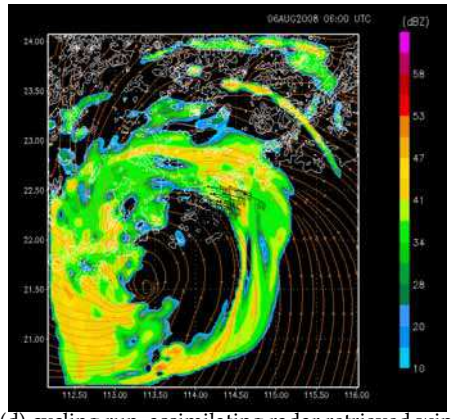

(d) cycling run, assimilating radar retrieved winds

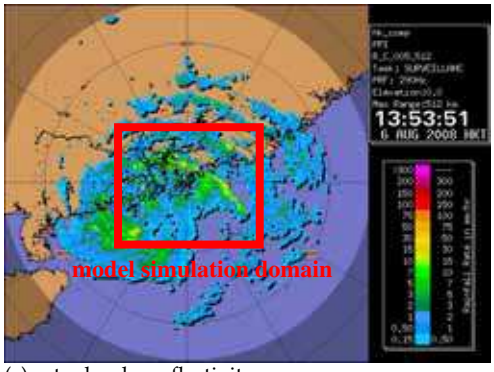

(e) actual radar reflectivity

Fig. 15. The simulated radar reflectivity (coloured contours) and streamlines for the four different model runs (a) to (d) at 06 UTC, 6 August 2008. (e) shows the actual radar reflectivity at the same time.

The operational mesoscale model of the Hong Kong Observatory has just been upgraded to a non-hydrostatic model. The horizontal resolution gets down to 2 km at the present, and would become sub-kilometre scale in the future. Assimilation of remote-sensing meteorological data, such as radars and satellites, is under development in the operational data assimilation suite. With the use of such a model setup for some time, more experience would be accumulated on kilometre scale to sub-kilometre scale simulation, advanced data assimilation, and the selection of the appropriate model physics. The results of the operational runs would be reported in the papers in the future.

7. References

Barker, D.M.; Huang, W., Guo, Y.R., & Xiao, Q.N. (2004). A three-dimensional (3DVAR) data assimilation system for use with MM5: Implementation and initial results. *Mon. Wea. Rev.*, 132, 897-914.

Brasseur, O. (2001). Development and application of a physical approach to estimating wind gusts. *Mon. Wea. Rev.*, 129, 5-25.

Chan, P.W. (2006). Generation of eddy dissipation rate map at the Hong Kong International Airport based on Doppler LIDAR data. *12th Conference on Aviation, Range, and Aerospace Meteorology*, Atlanta, GA, U.S.A.

Chan, P.W. (2009). Atmospheric Turbulence in Complex Terrain: Verifying numerical model results with observations by remote-sensing instruments. *Meteorol. Atmos. Phys.*, 103, 145-157.

Chan, P.W.; & Chan, S.T. (2004). Performance of eddy dissipation rate estimates from wind profilers in turbulence detection. *11th Conference on Aviation, Range, and Aerospace Meteorology*, Hyannis, MA, U.S.A.

Chan, S.T.; & Mok, C.W. (2004). Comparison of Doppler LIDAR observations of severe turbulence and aircraft data. *11th Conference on Aviation, Range, and Aerospace Meteorology*, Hyannis, MA, U.S.A.

Cheung, P.; Lam, C.C., & Chan, P.W. (2008). Numerical simulation of wind gusts in terrain-disrupted airflow at the Hong Kong International Airport. *13th Conference on Mountain Meteorology*, Whistler, BC, Canada.

Cheung, T.C.; & Chan, P.W. (2010). Improving wind and rain simulations for tropical cyclones with the assimilation of Doppler radar data. *The Open Atmospheric Science Journal*, 4, 57-63.

Clark, T.L.; Keller, T., Coen, J., Neilley, P., Hsu, H., & Hall, W.D. (1997). Terrain-induced turbulence over Lantau Island: 7 June 2004 Tropical Storm Russ case study. *J. Atmos. Sci.*, 54, 1795 – 1814.

Cotton, W.R.; Pielke Sr., R.A., Walko, R.L., Liston, G.E., Tremback, C., Jiang, H., McAnelly, R.L., Harrington, J.Y., Nicholls, M.E., Carrio, G.G, & McFadden, J.P. (2003). RAMS 2001: Current status and future directions. *Meteor. Atmos. Phys.*, 82, 5-29.

Deardorff, J.W. (1980). Stratocumulus-capped mixed layers derived from a three-dimensional model. *Bound.-Layer Meteor.*, 18, 495–527.

Fast., J.D.; & Shaw, W.J. (2002). An evaluation of mesoscale model predictions of turbulence kinetic energy and dissipation. VTMX Science Meeting, Salt Lake City, U.S.A., 17 – 19 September 2002 (http://www.pnl.gov/vtmx/presentations2002.html).

Geerts, B. (2001). Estimating downburst-related maximum surface wind speeds by means of proximity soundings in New South Wales, Australia. *Wea. Forecasting*, 16, 261-269.

HKO; IFALPA, & GAPAN (2010). *Windshear and Turbulence in Hong Kong – information for pilots*. 3nd Edition.

ICAO (2007). *Meteorological Service for International Air Navigation, Annex 3 to the Convention on International Civil Aviation (16th Edition)*, International Civil Aviation Organization.

Lam, C.C.; & Hilda Lam (2006). Analysis of high wind gusts associated with thunderstorms, tropical cyclones and monsoons. *20th Guangdong – Hong Kong – Macao Seminar on Meteorological Technology* (in Chinese with English abstract).

Mellor, G. L.; & Yamada, T. (1982). Development of a turbulence closure model for geophysical fluid problems. *Rev. Geophys. Space Phys.*, 20, 851–875.

Trini Castelli, S.; Ferrero, E., Anfossi, D., & Ohba, R. (2005). Turbulence closure models and their application in RAMS. *Environmental Fluid Mechanics*, 5, 169–192.

Xu, D.; & Taylor, P.A. (1997). On turbulence closure constants for atmospheric boundary-layer modelling: neutral stratification. *Boundary-Layer Meteorology*, 84, 267-287.

Yang, Y.; & Qiu, C.J. (2006). Analysis on mesoscale circulation within a heavy rain system using Doppler radar data. *Plateau Meteorology*, 25, 925-931 (in Chinese with English abstract).

Yeung, L.H.Y.; Chan, P.K.Y., & Lai, E.S.T. (2005). Impact of radar rainfall data assimilation on short-range quantitative precipitation forecasts using four-dimensional variational analysis technique. *32nd Conference on Radar Meteorology*, American Meteorological Society, New Mexico, U.S.A.

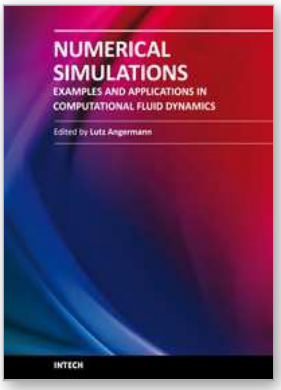

Numerical Simulations - Examples and Applications in Computational Fluid Dynamics

Edited by Prof. Lutz Angermann

ISBN 978-953-307-153-4
Hard cover, 440 pages
Publisher InTech
Published online 30, November, 2010
Published in print edition November, 2010

This book will interest researchers, scientists, engineers and graduate students in many disciplines, who make use of mathematical modeling and computer simulation. Although it represents only a small sample of the research activity on numerical simulations, the book will certainly serve as a valuable tool for researchers interested in getting involved in this multidisciplinary ï¬eld. It will be useful to encourage further experimental and theoretical researches in the above mentioned areas of numerical simulation.

How to reference

In order to correctly reference this scholarly work, feel free to copy and paste the following:

Pak Wai Chan (2010). Advanced Applications of Numerical Weather Prediction Models - Case Studies, Numerical Simulations - Examples and Applications in Computational Fluid Dynamics, Prof. Lutz Angermann (Ed.), ISBN: 978-953-307-153-4, InTech, Available from: http://www.intechopen.com/books/numerical-simulations-examples-and-applications-in-computational-fluid-dynamics/advanced-applications-of-numerical-weather-prediction-models-case-studies

INTECH
open science | open minds

InTech Europe
University Campus STeP Ri
Slavka Krautzeka 83/A
51000 Rijeka, Croatia
Phone: +385 (51) 770 447
Fax: +385 (51) 686 166
www.intechopen.com

InTech China
Unit 405, Office Block, Hotel Equatorial Shanghai
No.65, Yan An Road (West), Shanghai, 200040, China
中国上海市延安西路65号上海国际贵都大饭店办公楼405单元
Phone: +86-21-62489820
Fax: +86-21-62489821